

An edited version of this preprint was published by AGU. Copyright (2020) American Geophysical Union.
Link to publisher version with DOI: <https://doi.org/10.1029/2019JC015188>

1 **Relationships between Chlorophyll-a and Suspended**
2 **Sediment Concentration in a High-nutrient Load**
3 **Estuary: An Observational and Idealized Modeling**
4 **Approach**

5 Manuel Díez-Minguito¹, Huib E. de Swart²

6 ¹Andalusian Institute for Earth System Research (IISTA), University of Granada, Spain
7 ²Institute for Marine and Atmospheric Research (IMAU), Department of Physics, Utrecht University,
8 Netherlands

9 **Key Points:**

- 10 • Observed Chla concentration exhibited in-phase oscillations with the SSC at the
11 spring-neap and tidal scales, contrary to what occurred at larger time scales.
12 • Chla variability at these scales is hypothesized to be largely controlled by tidal
13 resuspension of microphytobenthos.
14 • Only at certain apogean neap tide periods did Chla observations vary during the
15 day-night cycle.
16 • An idealized 1DV model, which accounted for basic biotic and physical processes,
17 mimics and helps to explain the SSC-Chla relationships.

Corresponding author: Manuel Díez-Minguito, mdiezm@ugr.es

Abstract

The Guadalquivir estuary is a high-nutrient load environment, yet it has a reduced primary production because the high Suspended Sediment Concentration (SSC) causes light attenuation. High-resolution observations revealed relationships between the SSC and Chlorophyll-a (Chla) concentration from seasonal to intratidal time-scales. Local maxima of time-averaged Chla levels occurred at locations with relatively low SSC. In the upper (lower) part of the estuary, larger Chla concentrations were observed during the wet (dry) season. In contrast to longer time-scales, SSC and Chla exhibited in-phase oscillations during the spring-neap cycle. Both SSC and Chla were found to peak at maximum ebb and flood. There was no positive correlation at certain apogean neap tides, and instead Chla exhibited daily variations. An idealized model was developed, which mimicked and helped to explain the SSC-Chla relationships at different time scales. The model accounts for the vertical advection of Chla and SSC, tidal resuspension, radiation-mediated growth and effects of the change in stratification stemming from tides and SSC. The specific growth rate of the Chla biomass is inhibited due to high SSC levels throughout the year. The in-phase relationship at spring-neap and tidal scales seems to be due to resuspension of algal microorganisms attached to sediments. Daily variability of Chla during apogean neap tides emerges because tidal shear stress is low and the strong decline in the suspended particulate matter reduces the light attenuation. The light-mediated growth of part of the biomass, still remaining in the upper layers of the water column, is then driven by the day-night cycle.

Plain language abstract. Phytoplankton exist at the base of the aquatic food web. These microorganisms harvest light to produce oxygen and biomass through photosynthesis in the presence of nutrients. To elucidate their potential for producing biomass, it is important to understand how environmental conditions control phytoplankton growth. This knowledge is particularly relevant in reduced-growth environments, such as the Guadalquivir Estuary, which sustain high nutrient loads from the catchment. In this study, analyses of observations and idealized model experiments revealed the complex spatiotemporal variability of biomass induced by the joint action of tides, run-off and radiation. The attenuation of light due to the high levels of Suspended Sediment Concentration (SSC) hindered seasonal specific growth rates of biomass. However, SSC and Chlorophyll-a (Chla) fluorescence, which are widely regarded as measures of biomass content, did not always show an inverse relationship. Tidal resuspension caused SSC and Chla to peak at maximum ebb and flood. The large sinking velocities of Chla-containing matter that ensued from the model results analysis indicate that a substantial amount of biomass is composed of algal species that are attached to sediments. The results will allow a better understanding and evaluation of the biotic response of the estuary to future environmental changes.

1 Introduction

Phytoplankton form the base of the marine food web. These microorganisms are able to absorb light to convert inorganic carbon and water into oxygen and chemical energy through photosynthesis, thereby yielding the potential to increase their biomass (Cloern et al., 2014). The concentration of phytoplankton biomass is often quantified in terms of Chlorophyll-a (Chla), which is the primary molecule that is responsible for photosynthesis. Concentration of Chla is regarded as an indicator of water quality and a convenient proxy for the biomass content (e.g., Boyer et al. (2009)). In estuaries, however, the Chla concentration distribution is far from being uniform. The temporal and spatial variability of Chla concentration is primarily driven by light availability, nutrient supply, turbulent mixing, buoyancy input, and tidal and residual flows (e.g., Cloern (1996); Roegner et al. (2011)). Specifically, phytoplankton growth is limited by the availability of sunlight, nutrients input and by carbon. Temperature and salinity also affect photosynthetic

69 growth rates. The phytoplankton concentration decays because of losses caused by graz-
70 ing, respiration, sinking, and cell lysis triggered by osmotic stress (Cloern et al., 2014).

71 Light attenuation caused by Suspended Sediment Concentration (SSC) is one of
72 the main factors hampering the growth of biomass in estuaries (May et al., 2003; Mc-
73 Sweeney et al., 2017; Uncles et al., 2018). This phenomenon particularly occurs at Es-
74 tuarine Turbidity Maxima (ETM), i.e., locations where the SSC attains a maximum (Fisher
75 et al., 1988; Muylaert & Sabbe, 1999). The Ems, Gironde and Guadalquivir estuaries
76 are just three examples that exhibit ETM with low productivity (e.g., de Jonge et al.
77 (2014); Lajaunie-Salla et al. (2017); Ruiz et al. (2017)).

78 Stratification conditions play an important role in the temporal and spatial pat-
79 terns of phytoplankton (e.g., Roegner et al. (2011)). The intensity of turbulent mixing
80 depends on its production (mainly by tides) and its destruction by density stratification
81 (by temperature, salinity and SSC). The greater the stratification, the more the verti-
82 cal transfer of turbulence is suppressed (e.g., Geyer et al. (2000); Stacey and Ralston (2005)).
83 These processes impact SSC and Chla concentration patterns in estuaries, especially when
84 the stratification is strong (McSweeney et al., 2017; Liu & de Swart, 2018).

85 Observations and modeling of phytoplankton in estuaries exhibiting high SSC val-
86 ues have mainly focused on the occurrence of phytoplankton blooms and spatiotempo-
87 ral patterns at subtidal scales. Monismith et al. (1996) pointed out that currents in the
88 Suisun Bay can be sufficiently large to counter the sinking of some sediment and phy-
89 toplankton particles, thus causing relatively high concentrations of phytoplankton biomass
90 to be retained in the ETM. Muylaert and Sabbe (1999) reported relatively high Chla con-
91 centrations outside the ETM in the Elbe and Gironde estuaries. Differences in Chla con-
92 centration magnitudes between these estuaries were attributed to differences in SSC and
93 residence times. May et al. (2003) showed that the phytoplankton biomass had an in-
94 verse relationship with the SSC in the South San Francisco Bay. They found that blooms
95 could develop during neap tides due to net sediment deposition. Additionally, de Swart
96 et al. (2009) and Liu et al. (2018) studied the dynamics of phytoplankton blooms in sus-
97 pended sediment dominated estuaries at the subtidal scale. Model results revealed that
98 the joint variability of SSC and nutrients causes high growth rates of phytoplankton sea-
99 ward of the estuarine turbidity maximum. River flows, which to a large extent determine
100 the residence times, significantly influence the SSC distribution and ability of phytoplank-
101 ton to grow (L. V. Lucas et al., 2009; Azevedo et al., 2014).

102 The relationships between Chla and SSC at shorter, tidal scales have been stud-
103 ied less and pose problems that remain to be resolved. Processes that occur at the tidal
104 scale may impact the behavior of Chla at longer time scales (L. V. Lucas & Cloern, 2002).
105 Conversely, forcings that operate at seasonal and event scales (solar radiation, freshwa-
106 ter discharges) modulate tidal amplitudes and phases of Chla concentrations (Muylaert
107 et al., 2001). Therefore, quantitative evaluation of SSC-Chla variability at different time
108 scales is critical to gain basic knowledge of its dependence on external forcings.

109 Accordingly, the aim of this study was to provide a coherent view of the dependence
110 of the joint spatiotemporal variability of SSC and Chla on external forcings in estuar-
111 ine environments with reduced growth. In particular, the following research questions
112 were addressed:

- 113 1. To what extent do external forcings (i.e., solar radiation, freshwater discharge, and
114 tides) that operate at different time scales control the along-channel patterns of
115 Chla-containing biomass in estuaries?
- 116 2. What is the impact of the presence of suspended sediment on Chla variability, es-
117 pecially at spring-neap and intratidal time scales, under highly turbid conditions?
- 118 3. What is the quantitative impact of the joint action of tides and day-night radi-
119 ation cycles on possible SSC-Chla relationships?

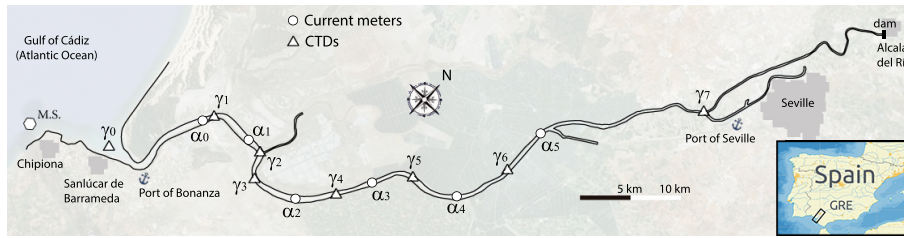


Figure 1. Study area ($36^{\circ}43'N - 37^{\circ}32'N, 5^{\circ}56'W - 6^{\circ}30'W$) with the locations of the sampling stations used in this study, namely, current meters (circles, α_k) and environmental sampling stations (triangles, γ_k). The label M.S. denotes the Meteorological Station off Chipiona.

120 To address the first and second research question, field data of turbidity, chloro-
 121 phyll fluorescence, currents and incoming solar radiation were analyzed in the Guadalquivir
 122 River Estuary (GRE). The GRE is a highly turbid environment that exhibits high-nutrient
 123 and low primary production rates because of the attenuation of light by the high SSC,
 124 even during low river flows. During such flow conditions, the estuary is weakly strati-
 125 fied in terms of salinity and temperature. A set of high-resolution data, which was au-
 126 tomatically collected between 2008 and 2011, was the basis for the analysis. Harmonic
 127 and wavelet analysis techniques were applied to the data to identify the joint modes of
 128 variability of SSC and Chla at different time scales.

129 To address the third research question, a highly idealized model was developed and
 130 analyzed. The purpose of this model was to capture and explain the main features of
 131 the observed variability of Chla and SSC. The idea is that, although this model is ap-
 132 plied to the GRE, it is generic in the sense that it can also be used to investigate Chla
 133 and SSC variability in other estuaries with high loads of suspended sediments and nu-
 134 trients.

135 The manuscript is organized as follows. Section 2 introduces the study area and
 136 presents the environmental conditions of the GRE. This section also describes the field
 137 data and methods to analyze them. Moreover, it presents the equations of the idealized
 138 model, including the applied assumptions and simplifications that are based on the GRE
 139 conditions and the design of the experiments. Section 3 contains the analysis of the field
 140 data and model results at different time scales. The physical and biotic processes derived
 141 from the analysis of the results, as well as the model limitations and capabilities, are dis-
 142 cussed in Section 4. The final Section contains the main conclusions of this study. Com-
 143 plementary details concerning the numerical scheme of the idealized model are presented
 144 in Appendix A.

145 2 Material and Methods

146 2.1 Study Area

147 The Guadalquivir River Estuary is a highly turbid coastal-plain estuary located
 148 in the south-western part of the Iberian Peninsula. The GRE comprises the last 110 km
 149 of the Guadalquivir, from its mouth where the river discharges into the Gulf of Cádiz
 150 (Atlantic Ocean) to the head dam at the town of Alcalá del Río (Fig. 1). The width of
 151 the estuary at the seaward boundary is approximately 800 m and it exponentially de-
 152 creases to 150 m at the landward end. Its mean depth, $h \approx 7$ m, is maintained by pe-
 153 riodic dredging to allow ships to reach the Port of Seville, located at 85 km from the es-
 154 tuary mouth. Tides are mesotidal and semidiurnal (tidal range at the mouth ~ 3.5 m
 155 in spring tides) and the M2 is the most significant component. Given that the estuary

156 is flood-dominated, it exhibits shorter, more intense floods and longer, weaker ebbs (Díez-
157 Minguito et al., 2012).

158 The climate in most of the Guadalquivir estuary catchment is Mediterranean. Rel-
159 atively short and intense freshwater discharges occur during the wet season (October–April),
160 typically after long periods of low river flows. The catchment, which is extensively reg-
161 ulated mostly because of agricultural activities, is over 63800 km². Freshwater discharges
162 from the Alcalá del Río dam are normally below 40 m³s⁻¹, although during extreme events
163 values exceeding 5000 m³s⁻¹ were recorded. The dam releases account for approximately
164 80% of the total fresh water input into the estuary.

165 Because salinity decreases upstream, the GRE is a positive estuary. Salinity records
166 indicate that the salt intrusion null-point barely reaches the Port of Seville. During low
167 river flows, the estuary is tidally energetic and weakly stratified in terms of salinity (Díez-
168 Minguito et al., 2013) and temperature (García-Lafuente et al., 2012), even during neap
169 tides, over most of its course.

170 The GRE plays an important role in the control of the biological productivity on
171 the shelf. Westerly winds, which favor upwelling, trigger seasonal Chla growth on the
172 shelf (Prieto et al., 2009). The GRE is subject to high anthropogenic inorganic nutri-
173 ent input, both from its agricultural catchment areas (González-Ortegón & Drake, 2012)
174 and surrounding urban areas hosting ~ 1.7 million inhabitants. According to Ruiz et
175 al. (2017), along-channel time-mean values of observed nitrate and phosphate concen-
176 trations are 282 mmol m⁻³ and 2.5 mmol m⁻³, respectively. These values are orders of
177 magnitude greater than those considered to be limiting for phytoplankton growth. How-
178 ever, organisms are unable to make use of all these nutrients because photosynthesis in
179 this estuary is severely restricted by limited light availability due to the large amount
180 of suspended sediments in the water column. Thus, the GRE is regarded as a reduced-
181 growth environment. Along-channel mean (most often) values of the Chla-containing biomass
182 concentration sampled *in-situ* are as low as 2.41 mg m⁻³ (0.8 mg m⁻³) (Ruiz et al., 2017).

183 2.2 Field Data

184 To evaluate how solar radiation, river flow, and tides control the spatiotemporal
185 patterns of Chla in a sediment-laden water column (first and second research question),
186 a harmonic and wavelet analysis of field data was performed on time series of chlorophyll
187 fluorescence, SSC and along-estuary current. Subsection 2.2.1 describes the data recorded
188 in the GRE and Subsection 2.2.2 explains the methodological aspects of the harmonic
189 and wavelet analysis techniques applied.

190 2.2.1 Data Sources

191 The data analyzed and discussed were recorded continuously by current profilers
192 and environmental probes during a field campaign from 2008 to 2011. Detailed techni-
193 cal descriptions of the equipment, as well as availability of data and plots showing time
194 series of the observations, were presented in Navarro et al. (2011). Only a brief descrip-
195 tion of the sampling stations and the data used in this study is given. Times in this work
196 are provided in mm/dd/yy format.

197 Acoustic Doppler Current Profilers were located at surface navigational buoys of
198 the Port of Seville along the thalweg. They are denoted by α_k , $k = 0, \dots, 5$ in Fig. 1.
199 Data regarding the currents at each location α_k were recorded every 15 min. Currents
200 are positive during flood and negative during ebb. There were eight environmental sam-
201 pling stations installed along the thalweg in other navigation aid buoys of the Port of
202 Seville. These devices, denoted as γ_k in Fig. 1, measured temperature, conductivity, tur-
203 bidity, dissolved oxygen and chlorophyll fluorescence every 30 min (during some periods
204 every 15 min) at $z = 1$ m below the water surface. Measurements up to $z = 4$ m were

205 available before October 2009. Station γ_0 , the seamount sampling station, was selected
 206 as the origin of the along-channel coordinate x , which is taken to represent positive land-
 207 ward direction.

208 In this study, the suspended sediment concentration is expressed in kg m^{-3} and val-
 209 ues were obtained from turbidity data in formazine nefelometric units (fmu). Calibra-
 210 tion of the samples established a relationship between the SSC and the fmu of $(1.60 \pm 0.15) \cdot$
 211 $10^{-3} \text{ kg m}^{-3} \text{ fmu}^{-1}$ (Navarro et al., 2011), where error bars represent the 95% confidence
 212 intervals. The fluid density ρ (sea water and suspended sediment mixture) was calcu-
 213 lated from the sea water density ρ_{sw} at the γ_k stations as $\rho = \rho_{sw} + (1 - \rho_{sw}/\rho_s)c$,
 214 where $\rho_s = 2650 \text{ kg m}^{-3}$ is the sediment density, c is the suspended sediment concen-
 215 tration and ρ_{sw} values are determined from the temperature, salinity and pressure data.
 216 Fluorimeters were prepared to obtain measurements in sediment-laden water (Navarro
 217 et al., 2011). According to these authors, fluorescence measurements (provided in rel-
 218 ative units, r.u.) are reliable for waters with turbidity values lower than 2.4 kg m^{-3} (1500 fmu).
 219 The SSC values analyzed in this study are below that threshold. These SSC values are
 220 typically observed during normal conditions corresponding to more than 75% of the days
 221 of the year.

222 The incoming radiation (Ω , in W m^{-2}) was obtained from the meteorological sta-
 223 tion installed on the Salmedina reef marker (M.S. in Fig. 1) located on the continental
 224 inner shelf off Chipiona. Freshwater discharge records from the upstream dam at Alcalá
 225 del Río, Q (m^3s^{-1}), were obtained from the Agencia de Medio Ambiente y Agua de An-
 226 dalucía [Regional Water Management Agency].

227 **2.2.2 Data Analysis Methods**

228 Assessment of the dependence of Chla and SSC on external forcings was mainly
 229 addressed by analysis of time series. Since a substantial part of the variability of Chla
 230 and SSC is controlled by tidal forcing, harmonic analysis was applied to the time series.
 231 This technique provides the amplitudes and phases of tidal constituents with known pe-
 232 riods. Harmonic analysis was performed on time series of the SSC and Chla concentra-
 233 tion using the T_TIDE package (Pawlowicz et al., 2002). The analysis interval comprised
 234 two spring-neap cycles from 08/01/08 to 09/07/08. This interval corresponded to sum-
 235 mer upwelling conditions at the seaward boundary and low river flows. The harmonic
 236 analysis focused on semidiurnal ($T_{M2} = 12.42 \text{ h}$, $T_{S2} = 12.00 \text{ h}$, $T_{N2} = 12.65 \text{ h}$) and
 237 quarter-diurnal ($T_{M4} = 6.21 \text{ h}$, $T_{MS4} = 6.10 \text{ h}$, $T_{MN4} = 6.26 \text{ h}$) constituents to capture
 238 the full spring-neap variability, including apogee-perigee variations in spring and neap
 239 tides and intratidal variability.

240 Relationships between Chla, SSC and external forcings, which were difficult to dis-
 241 cern from the time series or harmonic analysis (e.g., those of a nontidal origin), were in-
 242 ferred from wavelet analysis. Wavelet analysis resolves both frequency modes and vari-
 243 ations of these modes over time. The wavelet transform coherence detected similar fre-
 244 quencies in the variability of two time series and estimated their phase differences, whereas
 245 the cross wavelet transform provided the common power and relative phase between wavelet
 246 transforms of the two time series (e.g., Chla and SSC). Here, the wavelet coherence and
 247 cross wavelet transform by Grinsted et al. (2004) were applied. A Morlet-type wavelet
 248 function, with a dimensionless wavelet frequency set to 6 and a frequency resolution of
 249 $1/20$ (20 scales per octave), was used because of its optimal properties for feature ex-
 250 traction from biogeochemical time series (Grinsted et al., 2004). The analysis interval
 251 for wavelet analysis was from 10/24/09 to 11/08/09 as cross wavelet and coherence wavelet
 252 analyses required simultaneous availability of data of currents, Chla, SSC and radiation.

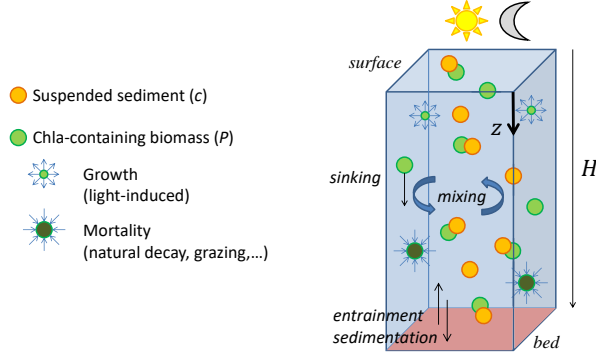


Figure 2. Sketch of the domain (vertical column of depth H) and of the processes considered in the idealized model. Growth of Chla-containing biomass is due to light (day-night cycle). The mortality rate is associated with natural decay or consumption. Sediment particles, which can convey Chla-containing biomass (symbols overlapped), sink because of gravity or are eroded and kept in suspension by tidal action.

253

2.3 Model

254

To address the third research question, a column model was developed and analyzed. Section 2.3.1 outlines the model and formulates its equations. Section 2.3.2 describes the experiments that explain prominent features of the Chla concentration and SSC variability in the GRE at seasonal, event, and spring-neap and tidal scales.

255

256

257

258

2.3.1 Basic Equations

259

The Chla concentration was calculated from the time-dependent and depth-dependent equation for advective and diffusive vertical transport, i.e., weak longitudinal advection is assumed. The model accounts for the influence of SSC on the Chla concentration, without separating the different Chla-containing species; all species are lumped in the Chla concentration. Chla-containing biomass does not affect SSC. Sources and sinks of phytoplankton biomass include solar radiation-mediated growth, mortality by natural decay or consumption, and entrainment by tidal shear stress (see Fig. 2). The equations for Chla and SSC are solved simultaneously as follows:

260

261

262

263

264

265

266

267

$$\frac{\partial P}{\partial t} = (\mu - \nu_P) P - w_{s,P} \frac{\partial P}{\partial z} + \frac{\partial}{\partial z} \left(K_v \frac{\partial P}{\partial z} \right), \quad (1a)$$

268

269

$$\frac{\partial c}{\partial t} = -w_{s,c} \frac{\partial c}{\partial z} + \frac{\partial}{\partial z} \left(K_v \frac{\partial c}{\partial z} \right). \quad (1b)$$

270

Here, t is time, z is the vertical coordinate ($z = 0$ at the surface), $P(z, t)$ denotes the Chla concentration (as a measure of phytoplankton biomass) and $c(z, t)$ is SSC. Sediment and Chla-containing matter have effective settling velocities $w_{s,c}$ and $w_{s,P}$, respectively. Dispersion is modeled by a vertically uniform eddy diffusivity coefficient K_v , which depends on the tidal velocity and thus on time. The local source term in the equation for the Chla concentration accounts for the competition between the specific growth and mortality with rates μ and ν_P , respectively. The difference between both, i.e. $\mu - \nu_P$, is defined as the net specific growth rate. The loss rate ν_P is assumed to be constant. The specific growth rate is given by

271

272

273

274

275

276

277

278

$$\mu(z, t) = \mu_{\max} [1 - \exp(-e_P I(z, t))], \quad (2)$$

279

280

281

282

where μ_{\max} is the maximum specific growth rate, which is assumed to be temperature-independent. The term $[1 - \exp(-e_P I(z, t))]$ limits growth with a photosynthetic efficiency e_P (Arndt et al., 2007). Since the Guadalquivir is a highly turbid, nutrient-rich

283 estuary throughout most of the year, primary production is assumed to be limited only
 284 by light. Light intensity I decays exponentially with depth z according to the Lambert-
 285 Beer law:

$$286 \quad I(z, t) = \Omega(t) \exp \left(-\kappa_w z - \kappa_P \int_0^z P(t, \zeta) d\zeta - \kappa_{SSC} \int_0^z c(t, \zeta) d\zeta \right), \quad (3)$$

287 which includes shading effects by water, phytoplankton, and sediments. Here, the con-
 288 stant κ_w is the light extinction coefficient due to light dispersion and absorption by wa-
 289 ter, κ_P is the light absorption coefficient due to P and κ_{SSC} is the light absorption co-
 290 efficient associated with c .

291 The incoming light intensity, $\Omega(t)$, which controls the day-night (daily) cycle of phy-
 292 toplankton, is modeled as follows:

$$293 \quad \Omega(t) = \begin{cases} (1 - a)S \sin(\Psi) & \text{during daytime} \\ 0 & \text{during nighttime,} \end{cases} \quad (4)$$

294 where a is the albedo and $S = 1368 \text{ W m}^{-2}$ is the solar constant. The local elevation
 295 angle of the Sun is Ψ , which is defined at a location with geographic coordinates (lon, lat)
 296 as

$$297 \quad \sin(\Psi) = \sin(\text{lat}) \sin(\delta_s) - \cos(\text{lat}) \cos(\delta_s) \cos(2\pi t - \text{lon}). \quad (5)$$

298 In this expression, $\delta_s = \Phi_r \cos(2\pi(t - 173)/365)$, with t expressed in days, and $\Phi_r =$
 299 23.45° is the axial tilt of the Earth's axis relative to the ecliptic. This formulation es-
 300 timates seasonal and daily variations in net incoming radiation, including daytime sea-
 301 sonal variation.

302 Equations 1a and 1b are complemented with two initial vertical distributions for
 303 P and c and four boundary conditions. The initial vertical profiles are the correspond-
 304 ing (theoretical) equilibrium solutions that obey the boundary conditions. The bound-
 305 ary conditions at the surface $z = 0$ and bed $z = H$ read

$$306 \quad K_v \frac{\partial P}{\partial z} = w_{s,P} P \quad \text{at } z = 0, \quad (6a)$$

$$307 \quad K_v \frac{\partial c}{\partial z} = w_{s,c} c \quad \text{at } z = 0, \quad (6b)$$

$$308 \quad K_v \frac{\partial P}{\partial z} = b_P \max\{\tau_b - \tau_c, 0\} \quad \text{at } z = H, \quad (6c)$$

$$309 \quad K_v \frac{\partial c}{\partial z} = b_c \max\{\tau_b - \tau_c, 0\} \quad \text{at } z = H. \quad (6d)$$

310 Boundary conditions 6a and 6b state the condition for zero-fluxes at the surface for P
 311 and c , respectively. Bottom boundary conditions 6c and 6d specify erosive fluxes of Chla
 312 and sediments at the bottom by tidal shear stress (Winterwerp & van Kesteren, 2004).
 313 The boundary-layer formulation for cohesive sediments of Sanford and Halka (1993) and
 314 Son and Hsu (2011) is adopted in Eqs. 6c and 6d. The time-dependent bottom shear stress,
 315 $\tau_b(t)$, and critical shear stress, $\tau_c(t)$, are estimated empirically, respectively, as follows:

$$316 \quad \tau_b(t) = \rho C_D u(t)^2, \quad (7a)$$

$$317 \quad \tau_c(t) = \alpha_1 \max\{m(t) - \alpha_2, 0\}. \quad (7b)$$

319 The critical shear stress (Eq. 7b) is parametrized as a function of the total suspended
 320 mass per unit area, $m(t) = \int_0^H c dz$, to account for bed consolidation effects, i.e., the
 321 larger the eroded sediment, the larger is τ_c . Parameters α_1 , α_2 , and C_D are local pos-
 322 itive empirical constants. The mass transfer efficiency parameters b_P and b_c in Eqs. 6c

323 and 6d represent the efficiency of the tidal current to erode Chla-containing and sedi-
 324 ment matter from the bottom and are considered independent of time.

325 Since the analysis of the influence of tides focused on spring-neap and tidal scales,
 326 including variations at the apogee-perigee time scale, current $u(t)$ was assumed a linear
 327 superposition of the main semidiurnal tidal constituents (M2, S2, and N2) and their most
 328 energetic overtones (M4, MS4, and MN4). This reads

$$329 \quad u(t) = \sum_{k=\{M2,S2,N2, \\ M4,MS4,MN4\}} u_k \cos(\omega_k t - \phi_k). \quad (8)$$

330 The superposition of the M2, S2, and N2 constituents reproduces the spring-neap cy-
 331 cle, including its 28.46 days of modulation due to the perigean and apogean tides caused
 332 by ellipticity of the lunar orbit (Dronkers, 1964). Their main overtones, M4, MS4, and
 333 MN4, account for the (intra-) tidal asymmetry.

334 The eddy diffusivity coefficient K_v includes the effects of tidal turbulent mixing and
 335 change in stratification caused by the tides and suspended sediment concentration. Ex-
 336 tending the Munk and Anderson (1948) formulation to the tidal time scale, the eddy dif-
 337 fusivity coefficient is

$$338 \quad K_v(t) = K_{v0} (1 + 10 Ri/3)^{-3/2}. \quad (9)$$

339 According to Bowden et al. (1959), the vertical eddy diffusivity when $Ri = 0$ is $K_{v0}(t) =$
 340 $C_V |u| H$, with $C_V = C_{VB} \pi/2$ and $C_{VB} \sim 1.6 \cdot 10^{-3}$ an empirical parameter. Since
 341 K_v is vertically uniform, the effects of stratification on this parameter are related to a
 342 bulk Richardson number Ri (e.g., Huijts et al. (2006)) rather than a gradient Richard-
 343 son number (as used by Munk and Anderson (1948)). The bulk Richardson number is
 344 defined as $Ri(t) = gH\Delta\rho / (\rho_b u^2)$, with $\Delta\rho(t)$ being a typical bottom-surface density
 345 difference that varies with the sediment concentration $c(z, t)$. To prevent Ri from increas-
 346 ing towards infinity at slack tides, a lower background limit for u is prescribed, viz. $0.01u_{M2}$.

347 **2.3.2 Design of Experiments**

348 Two series of experiments were designed to explain observations and assess the im-
 349 pact of the joint action of solar radiation and tides on the SSC-Chla variability at dif-
 350 ferent time scales (third research question). Each experiment addressed variability at the
 351 seasonal and spring-neap and tidal scales, respectively.

352 A first series of experiments was carried out to verify the ability of the idealized
 353 model to capture the main features of the low-frequency, seasonal variability of the Chla
 354 concentration and to evaluate the effect of SSC on the seasonal limitation of growth due
 355 to the attenuation of light. The low-frequency seasonal variability of both the net spe-
 356 cific growth rate and radiation were obtained by applying a 40-day low-pass filter to the
 357 simulated time series that resulted from unfiltered forcing. Spring-neap variability was
 358 thus filtered out, while preserving the contribution of the non-linear effect of short-term
 359 variations on the long-term variability. Five complete natural years beginning in 11/14/09
 360 were simulated. Sensitivity experiments with different maximum specific growth rates
 361 μ_{\max} and with and without light attenuation by SSC were performed. The second se-
 362 ries of experiments was carried out to investigate the relationship between SSC and Chla
 363 at the fortnightly and tidal scale. The simulations involved several full spring-neap cy-
 364 cles, including apogee-perigee variations in spring and neap tides.

365 The following approaches are common to all experiments. The conditions for the
 366 experiments were those during the 2009 field campaign in the lower part of the estuary.
 367 All experiments included forcing by solar radiation and by tides. The physical and bi-
 368 otic parameter values of the model were chosen within their typical ranges or adopted

Table 1. List of model parameters and default values, which are taken from the literature of the set according to the transport and dynamical characteristics of the lower part of the GRE.

Parameter	Definition	Value
H	Mean water depth ^a	7 m
g	Gravitational acceleration	9.8 m s^{-2}
ω_{M2}	M2 tidal frequency	$2\pi/12.42 \text{ h}^{-1}$
ω_{S2}	S2 tidal frequency	$2\pi/12.00 \text{ h}^{-1}$
ω_{N2}	N2 tidal frequency	$2\pi/12.65 \text{ h}^{-1}$
ω_{M4}	M4 tidal frequency	$2\omega_{M2}$
ω_{MS4}	MS4 tidal frequency	$\omega_{M2} + \omega_{S2}$
ω_{MN4}	MN4 tidal frequency	$\omega_{M2} + \omega_{N2}$
u_{M2}	M2 tidal current amplitude ^a	1.00 m s^{-1}
u_{S2}	S2 tidal current amplitude ^a	0.35 m s^{-1}
u_{N2}	N2 tidal current amplitude ^a	0.12 m s^{-1}
u_{M4}	M4 tidal current amplitude ^a	0.039 m s^{-1}
u_{MS4}	MS4 tidal current amplitude ^a	0.042 m s^{-1}
u_{MN4}	MN4 tidal current amplitude ^a	0.018 m s^{-1}
ϕ_{M2}	M2 tidal current phase ^a	63°
ϕ_{S2}	S2 tidal current phase ^a	80°
ϕ_{N2}	N2 tidal current phase ^a	20°
ϕ_{M4}	M4 tidal current phase ^a	100°
ϕ_{MS4}	MS4 tidal current phase ^a	97°
ϕ_{MN4}	MN4 tidal current phase ^a	70°
$\rho_{sw,sur}$	Sea water density at the surface ^b	$1005.89 \text{ kg m}^{-3}$
$\Delta\rho_{sw}$	Typical sea water density difference ^b	1.75 kg m^{-3}
$w_{s,c}$	Settling velocity for sediments ^c	$4.5 \cdot 10^{-4} \text{ m s}^{-1}$
b_c	Entrainment efficiency for sediments ^d	$1.0 \text{ s m}^2 \text{ kg}^{-1}$
$w_{s,P}$	Settling velocity for Chla ^c	$3.5 \cdot 10^{-4} \text{ m s}^{-1}$
b_P	Entrainment efficiency for Chla-containing biomass ^d	$0.50 \text{ s m}^2 \text{ kg}^{-1}$
C_D	Shear stress parameter ^a	$2.5 \cdot 10^{-3}$
α_1	Parameter in critical shear stress ^e	0.45 m s^{-2}
α_2	Parameter in critical shear stress ^e	0.05 kg m^{-2}
C_{VB}	Parameter in vertical eddy viscosity ^f	$1.6 \cdot 10^{-3}$
Φ_r	Axial tilt of the Earth	23.45°
lon	Longitude	6.25°W
lat	Latitude	36.89°N
S	Solar constant	1368 W m^{-2}
a	Albedo ^g	0.2
κ_w	Background light attenuation of water ^c	0.01 m^{-1}
κ_P	Coefficient of light absorption by Chla-containing matter ^h	$0.017 \text{ m}^2 \text{ kg}^{-1}$
κ_{SSC}	Coefficient of light absorption by SSC ⁱ	$1.8 \text{ m}^2 \text{ kg}^{-1}$
μ_{max}	Maximum specific growth rate of Chla ^c	0.1 h^{-1}
e_P	Photosynthetic efficiency ^j	$10^{-3} \text{ m}^2 \text{ W}^{-1}$
ν_P	Specific loss rate of Chla ^k	0.01 h^{-1}

^(a) Díez-Minguito et al. (2012).^(b) Díez-Minguito et al. (2014).^(c) Derived from data of Colijn and de Jonge (1984); Sarthou et al. (2005).^(d) Fitted to mimic observations.^(e) Son and Hsu (2011).^(f) Bowden et al. (1959).^(g) Best fit value to match incoming radiation from Eq. 4 and observations at M.S.^(h) Estimated from Ruiz et al. (2013).⁽ⁱ⁾ Branco and Kremer (2005).^(j) Estimated from Arndt et al. (2007).^(k) Sarthou et al. (2005).

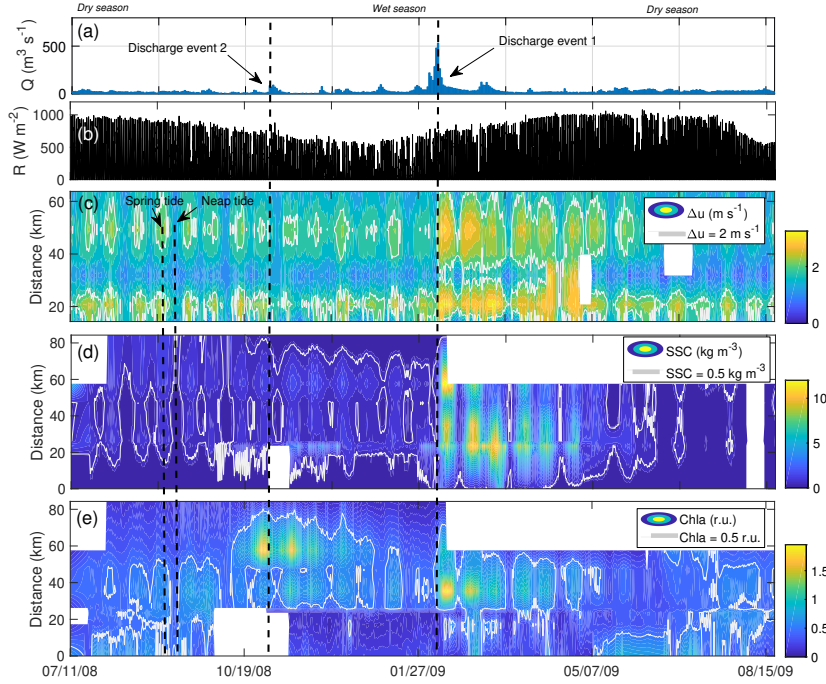


Figure 3. From top to bottom: Time series of recorded freshwater discharge (blue curve, left vertical axis) at the Alcalá del Río head dam (panel a). Observed net incoming radiation at the meteorological station (panel b). Observed spatiotemporal patterns at the near-surface of the current range, i.e., difference between the maximum flood current (positive) and maximum ebb current (negative) in a tidal cycle (panel c), tidally-averaged Suspended Sediment Concentration (panel d) and Chlorophyll-a (panel e). The vertical dashed lines indicate two consecutive neap and spring tides and the peak discharges of the events discussed in the main text. Light grey curves in panels c, d, and e represent contour lines for the values indicated in the corresponding legends. Blanked out parts of these panels refer to missing data.

369 from previous work in the literature. Table 1 shows the default parameter values of the
 370 model. More specifically, tidal currents for any period simulated were reconstructed using
 371 harmonic analysis techniques. The Chla concentration and SSC fields were obtained
 372 by numerically integrating Eqs. 1a and 1b. The study used a finite difference scheme,
 373 which is forward in time and centered in space. Details of the numerical scheme are given
 374 in Appendix A.

375 **3 Results**

376 **3.1 Field Data**

377 **3.1.1 Seasonal Variability**

378 The low-frequency, seasonal patterns of SSC and Chla are revealed in Fig. 3. This
 379 figure shows the time series of freshwater discharge (panel a) and radiation (panel b).
 380 It further shows Hovmöller diagrams of the tidal current range, being the difference
 381 between the maximum flood current (positive) and maximum ebb current (negative) in a
 382 tidal cycle (panel c), SSC (panel d) and Chla near the surface (panel e). The patterns
 383 of SSC and Chla show low-frequency, seasonal oscillations. Without considering the con-
 384 tribution to SSC by specific high-discharge events, the along-channel distribution of SSC
 385 (Fig. 3, panel d) was displaced approximately 10 km seaward during the wet season (October-
 386 April) in comparison to the dry season (May-September). During the wet season, the

387 SSC accumulated between 5 km and 70 km, whereas during the dry season, SSC extended
388 mainly from 10 km to 85 km.

389 Two ETMs that persist throughout the year were identified by Díez-Minguito et
390 al. (2014). The lowermost ETM was located around km 25. The uppermost, primary ETM
391 showed the highest tidally-averaged mid-depth concentrations (2.2 kg m^{-3} at km 57 dur-
392 ing low river flows), which were one order of magnitude over the values computed at the
393 mouth. The location of both ETMs varied between dry and wet seasons, being slightly
394 more downstream in the wet season.

395 The seasonal cycle of Chla patterns depended on the location along the estuary (panel e,
396 Fig. 3). The sections closest to the mouth exhibited larger averaged Chla concentrations
397 during the dry season, when light intensity is high (panel b, Fig. 3), than during the wet
398 season. Upstream stretches ($x > 25 \text{ km}$) reflected the opposite behavior. The Chla con-
399 centration had lower values during the summer than during winter.

400 *3.1.2 Spring-Neap and Tidal Variability*

401 *Time Series*

402 The modulation of amplitudes indicates a positive relationship between near-surface
403 currents, SSC and Chla at the fortnightly scale during low river flows. As evidenced by
404 higher current ranges (Fig. 4, panel a), larger tidal shear stress during spring tides led
405 to an increase in SSC (Fig. 4, panel b). More suspended sediment was observed at spring
406 tides than at neap tides. Interestingly, the higher Chla concentration values (Fig. 4, panel c)
407 also occurred at spring tide, but not at neap tide when turbidity was lower (panel b).
408 These observations showed that the Chla concentrations inside the GRE were in-phase
409 with the currents at the spring-neap tidal cycle and thus with SSC. Furthermore, SSC
410 and Chla concentrations exhibited in-phase oscillations within the tidal cycle (see the
411 vertical dashed lines in the figure).

412 Both suspended sediment and Chla concentrations typically peaked at maximum
413 ebb and flood, when the tidal bed shear stresses were large. Higher values occurred more
414 frequently during floods than during ebbs because of the fact that tidal currents are asym-
415 metric. This behavior was also observed in the time series of SSC and Chla at mid-depth
416 (dark-colored curves in insets b1 and c1, respectively). Furthermore, note that mid-depth
417 concentrations of both SSC and Chla were typically higher than those near the surface.
418 Only when currents were very low, and SSC in the water column was also low, was the
419 tidal in-phase oscillation of SSC and Chla lost. This occurred most clearly in the period
420 of apogean neap tides (black dashed boxes in Fig. 4), during which the Chla concentra-
421 tion generally varied on a daily basis.

422 *Harmonic Analysis*

423 Figure 5 shows the M2 semidiurnal and M4 quarter-diurnal harmonic constants of
424 the SSC and Chla at different locations along the main channel. Time averages during
425 the same analysis interval (from 08/01/08 to 09/07/08) are also shown as a reference for
426 each variable (brown curve in panel a and green curve in panel b, respectively). Over-
427 all, the averaged SSC values were found to increase upstream (Fig. 5, panel a), whereas
428 Chla values decreased, depending on the distance to the mouth (panel b). Mean Chla
429 concentrations showed a mild decrease upstream until $x = 17 \text{ km}$, where a local mini-
430 mum was reached. Local maxima were attained at the mouth and further upstream ($x \gtrsim$
431 35 km). After that, mean Chla concentrations steadily declined. Local maxima of aver-
432 aged Chla levels occurred approximately in locations with relatively low SSC values,
433 i.e., between the two ETMs.

434 The second row of panels in Fig. 5 shows M2 semidiurnal tidal amplitudes (solid
435 curves) and phases (dashed curves) of SSC (panel c, brown curves) and Chla (panel d,

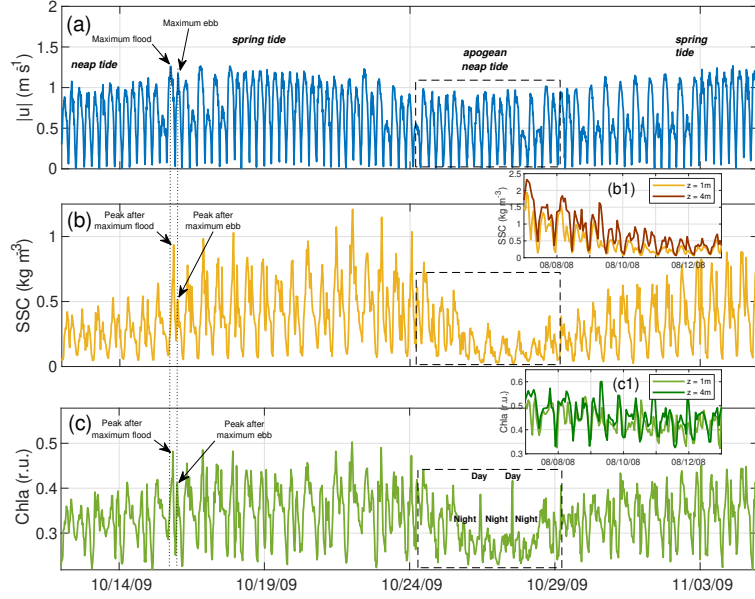


Figure 4. Time series at spring-neap and tidal time scales of the magnitude of the current, $|u|$, at station α_1 (panel a, blue curve), SSC at γ_3 (panel b, brown curve) and Chla at γ_3 (panel c, green curve). In these panels, near-surface values are shown. Labeled arrows indicate times of maximum flood and successive maximum ebb. Other labels indicate day-night and spring-neap periods. The black boxes show the behavior during the apogean neap tide period. Insets b1 and c1 show available time series of SSC and Chla, respectively, near the surface at $z = 1$ m (light-colored curves) and at $z = 4$ m (dark-colored curves).

436 green curves). Only the M2 constituent is shown and discussed here, since the behavior
 437 of the other semidiurnal constituents (S2 and N2) is similar to that of M2. Tidal am-
 438 plitudes of the SSC M2 constituent showed local maxima at $x = 84$ km and $x = 25$ km,
 439 which coincide with the locations of the two ETM. The maximum Chla M2 amplitude
 440 occurred at the mouth (panel d). Chlorophyll-a M2 amplitudes tended to decline strongly
 441 upstream. Secondary maxima of Chla M2 amplitude occurred at ETM locations. Sim-
 442 ilarly to what occurs with the SSC, these maxima could not be attributed to M2 advec-
 443 tion of the mean Chla concentration (except perhaps at the land-most station at $x =$
 444 84 km), but instead they were likely caused by a local source of Chla. Remarkably, the
 445 semidiurnal phases of the SSC and Chla (orange curves in panels c and d, respectively)
 446 had almost exactly the same values, with the notable exception of the station at the mouth.

447 Regarding the overtides (panels e and f in Fig. 5), the SSC and Chla quarter-diurnal
 448 amplitudes reached their maxima between the two ETMs. Suspended sediment and Chla
 449 M4 amplitude values were comparable to their respective semidiurnal values. The lon-
 450 gitudinal distribution of quarter-diurnal phases of the SSC and Chla (orange curves) be-
 451 behaved identically, i.e., they increased upstream and showed the same values, indicating
 452 that the Chla and SSC overtides were in phase. In other words, the highest Chla val-
 453 ues at intratidal scale were observed when SSC in the water column was also high.

454 **Wavelet Analysis**

455 Figure 6 shows wavelet coherence and cross-correlation between time series of cur-
 456 rent magnitude, Chla, SSC and incoming radiation. Regarding the relationship between
 457 the current magnitude and Chla concentration (panel a), the coherence and cross-correlation
 458 between the two time series during spring tides (panels b and c, respectively) was sig-
 459 nificant at semidiurnal periods and was especially significant during quarter-diurnal pe-
 460 riods. Phase lags at quarter-diurnal and semidiurnal were also similar to those of cur-

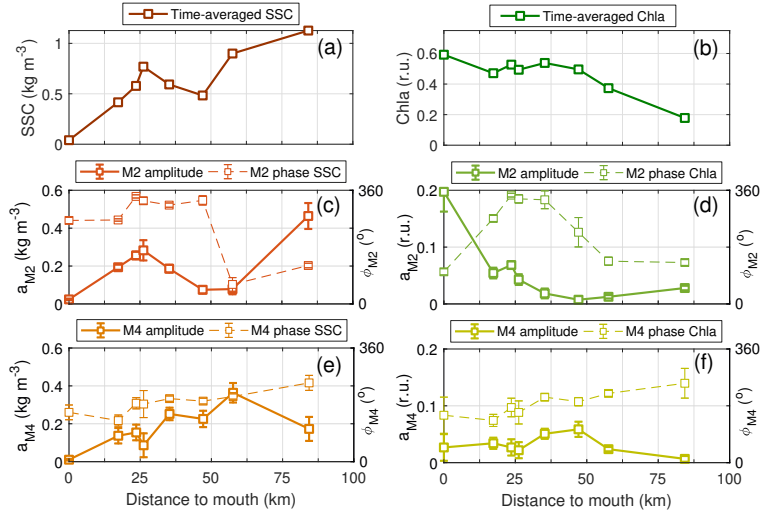


Figure 5. Panels a and b: Longitudinal distribution of time-averaged values of SSC and Chla, respectively. Error bars, which are estimated as four times the standard error, are smaller than the symbol sizes. Panels c and d: as in panels a and b, but for the M2 amplitudes and phases of SSC and Chla, respectively. Left vertical axes label tidal amplitudes, a_{M2} , (solid curves) and right vertical axes label tidal phases, ϕ_{M2} (dashed curves). Error bars in tidal amplitudes and phases represent the 95% confidence interval provided by the harmonic analysis. Panels e and f: As in panels c and d, except for the M4 constituent. Brown (green) curves in all panels are for SSC (Chla) values. The analysis interval was the same for all panels and consisted of two spring-neap cycles from 08/01/08 to 09/07/08. All panels show data near the surface.

461 rent and SSC. This finding supports earlier results of the harmonic analysis indicating
 462 that Chla variability seemed to be driven by tidal currents during these periods. How-
 463 ever, power coherence and cross-correlation at ~ 12 h and ~ 6 h were much weaker dur-
 464 ing the (apogean) neap tide (before 10/29/09) when currents and shear stress were lower.
 465 Coherence at the diurnal frequency was statistically significant at neap tide (panel b).
 466 The contributions to Chla variability induced by diurnal tides were less significant than
 467 those induced by semidiurnal and quarter-diurnal tides. Phase lags between diurnal and
 468 lower time scales differed by as much as 90° , which indicated a nontidal generating mech-
 469 anism of Chla concentration at the diurnal scale.

470 Coherence between SSC and Chla time series (panel d) was very high. In fact, sta-
 471 tistically significant values close to 1 were found at almost all ranges in the time-frequency
 472 space (panel e). A remarkable exception occurred during the apogean neap tide, when
 473 both coherence and correlation between SSC and Chla vanished. The highest cross-correlation
 474 values occurred at the same frequencies as for the current-Chla time series (panel f). Fur-
 475 thermore, there were hardly phase lags between both time series when coherence or cross-
 476 correlation was high, as revealed by panels e and f. Hence, SSC-Chla were in-phase ex-
 477 cept during the apogean neap tide.

478 Regarding the incoming solar radiation and Chla concentrations (panel g), both
 479 signals exhibited high coherence and had a positive correlation during the whole inter-
 480 val at the diurnal time scale without any noticeable phase lag (panels h and i). The per-
 481 sistent statistically significant correlations between Ω and Chla emerged at the apogean
 482 neap tide, which indicated Chla oscillations related to the day-night solar radiation cy-
 483 cle.

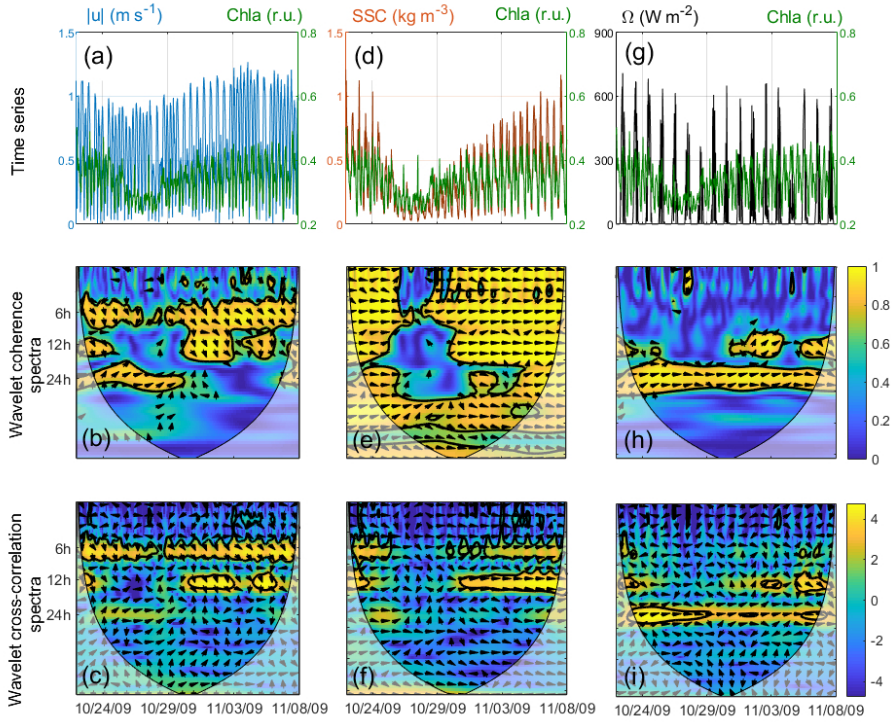


Figure 6. Panels a, b, and c show time series of the absolute value of the near-surface current at station α_1 (blue curve) and of Chla (green curve) at station γ_3 , a color plot of their wavelet coherence spectrum and a color plot of their wavelet cross-correlation spectrum, respectively. Panels d, e, and f: As in panels a, b, and c, except for SSC (brown curve) and Chla (green curve) at station γ_3 . Panels g, h, and i: As in panels a, b, and c, except for radiation Ω (black curve) at station M.S. and Chla (green curve) at station γ_3 . Warm colors indicate high coherence and high common power in the wavelet coherence and cross-correlation spectra, respectively. Thick black lines encircle 95% statistically significant regions of the spectra. Arrows indicate phase lags between the time series, viz. in-phase if pointing right, anti-phase if pointing left, and $+90^\circ$ -phase lag leading the first variable if pointing downward.

484

3.1.3 Variability prior and after High-discharge Events

485

486

487

488

489

490

491

492

493

494

495

496

497

498

499

500

Figure 3 also shows that freshwater discharge events may disrupt the low-frequency seasonal variability of Chla and SSC. During the high-discharge event with its peak at 02/07/09 (event 1, which started at 01/27/09, in panel a of Fig. 3), the larger volume of freshwater released from the dam (peak discharge of $Q \approx 531 \text{ m}^3\text{s}^{-1}$) apparently triggered high tidal currents, SSC and Chla concentration values (panels c, d, and e). The discharge event resulted in tidally-averaged SSC values at spring tides of $\sim 12 \text{ kg m}^{-3}$, which were at least one order of magnitude greater than those recorded under normal conditions in almost the entire estuary ($\sim 0.5 \text{ kg m}^{-3}$). The sediments were apparently kept in suspension by enhanced tidal currents (panel c). Similarly, Chla concentration values after event 1, particularly those observed near $x = 35 \text{ km}$, were significantly higher than during normal conditions (panel e). The increase in Chla after the high-discharge event was followed by a severe depletion of dissolved oxygen (not shown), thus pointing to enhanced oxygen consumption rates that were not compensated by primary production. The post-discharge adjustment of Chla to return to former levels took about 60 days. This period was apparently shorter than the adjustment time of currents (panel c) and SSC (panel d).

501

502

503

504

505

506

507

508

High Chla concentrations were also observed in the upper part of the estuary prior and after to high-discharge event 2 (peak discharge of $Q \approx 91 \text{ m}^3\text{s}^{-1}$ at 11/02/08). These enhanced values of Chla were observed further upstream, viz. km 60, and their intensities were slightly lower than those related to discharge event 1 (panel e). The spring-neap modulation and the adjustment period of the Chla concentrations toward their normal values were, however, similar to those of event 1. Event 2, with a discharge that was about six times weaker than that of event 1, did not have a noticeable impact on tidal currents and SSC (panels c and d, respectively).

509

3.2 Model Experiments

510

3.2.1 Seasonal Variability

511

512

513

514

515

Figure 7 (panel a) shows the relationship between the (low-frequency) seasonal net specific growth rate, $\mu - \nu_P$, and incoming solar radiation, Ω , near the bed, which is the most limiting location for growth. The results of the experiments show that, both with and without light attenuation, $\mu - \nu_P$ increases with radiation because the greater light intensity during summer favored growth.

516

517

518

519

520

521

522

523

524

525

526

As ν_P is constant, changes in the net specific growth rate are thus only due to variations in the specific growth rate μ . The difference in the net specific growth rate between summer and winter increases with increasing values of μ_{max} , i.e., the slope of the curves increases with μ_{max} . These differences are relatively smaller with suspended sediment (dotted curves) than without sediments (hollow symbols) in the water column. For example, for $\mu_{\text{max}} = 0.10 \text{ h}^{-1}$, the net specific growth rate $\mu - \nu_P$ near the bed increases in magnitude from winter to summer by approximately 0.001 h^{-1} for the case with light attenuation by SSC and by approximately 0.016 h^{-1} , i.e. a tenfold of the previous value, when SSC was switched off (squares). The presence of sediment hinders growth. Without considering sediments in the water column, the growth intensifies during summer and thereby, summer-winter differences are in that case more marked.

527

528

529

530

531

532

533

Regarding the vertical variability, note that for cases with light attenuation by SSC and the typical values of μ_{max} shown in panel a (dotted curves), the low-frequency net specific growth rate is negative at the bottom throughout the year, even during summer when light intensities are high. However, this behavior is only representative for the bottom, not for the whole water column. Therefore, panels b1 and b2 of Fig. 7 show the relationship between $\mu - \nu_P$ and Ω near the surface and near the bed, respectively, including light attenuation by SSC, while panel b3 shows the relation between the depth-averaged

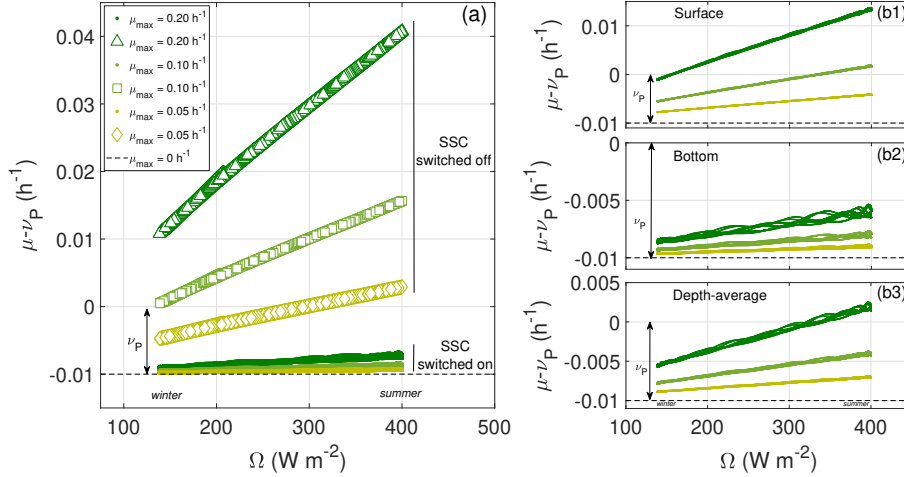


Figure 7. Long-term seasonal variability of the relationship between the net specific growth rate, $\mu - \nu_P$, and solar radiation, Ω , obtained from simulations of 5 years from 11/14/09. Panel a: Relationship near the bed at $z/H = 0.93$, for different maximum specific growth rate values, $\mu_{\max} = 0.05 \text{ h}^{-1}$, 0.10 h^{-1} , 0.20 h^{-1} , with light attenuation by SSC switched off ($\kappa_{\text{SSC}} = 0$, hollow symbols) and on ($\kappa_{\text{SSC}} = 1.8 \text{ m}^2 \text{ kg}^{-1}$, dots) (legend indicates colors and symbols). Panels b1 and b2: Relationship between $\mu - \nu_P$ and Ω near the surface at $z/H = 0.07$ and near the bed at $z/H = 0.93$, respectively, for the same μ_{\max} values with light attenuation by SSC switched on. Panel b3: as b1 and b2, but for the depth-averaged specific growth rate. The limit case for $\mu_{\max} = 0$ is shown in all panels for reference (black dashed lines). Default values of the model parameters are presented in Table 1.

534 specific growth rate and solar radiation. Model output shows that it is possible for the
 535 estuary to have positive net specific growth rates near the surface (panel b1), but nega-
 536 tive growth rates at the bottom (panel b2). This occurs in particular for $\mu_{\max} = 0.20 \text{ h}^{-1}$
 537 throughout the year, and for $\mu_{\max} = 0.10 \text{ h}^{-1}$ during summer ($\Omega > 320 \text{ W m}^{-2}$). Mod-
 538 elled depth-averaged net specific growth rates (panel b3) are found to be negative for
 539 all maximum specific growth rates explored, except for the highest rate $\mu_{\max} = 0.20 \text{ h}^{-1}$
 540 during summer ($\Omega > 300 \text{ W m}^{-2}$). Overall, model results indicate that the depth-averaged
 541 net specific growth rate contributes negatively to the local storage rate of P .

542 3.2.2 Spring-Neap and Tidal Variability

543 The spring-neap and tidal variability in modeled time series of SSC and Chla con-
 544 centration (Fig. 8) is similar to that in the observations described earlier. The results
 545 show higher concentrations of SSC during spring tides than during neap tides (panel a).
 546 The largest values of SSC occur near the bottom (dark brown curve). The bed shear stress
 547 erodes sediment from the bottom and this material is subsequently transported verti-
 548 cally in the water column by mixing. The largest values within the tidal cycle occur af-
 549 ter maximum flood due to the intratidal asymmetry induced by overtides. Concentra-
 550 tions near the surface (light brown curve) are lower and peak 15 min after those near
 551 the bed because of the mixing lag. A settling time lag between the tidal forcing and SSC
 552 occurs after low and high water slacks. The fast decay of SSC near the surface after slacks
 553 yields a relatively slower decay of SSC near the bottom with respect to near the surface.

554 Chlorophyll-a attains its largest concentration values at spring tide (panel b of Fig. 8),
 555 as in the observations. During spring tides, net specific growth rates appear to be tem-
 556 pered by turbidity (panel c). Part of the upper water column experiences positive net
 557 specific growth rates during daylight (panel c). However, tidal shear stress, which resus-
 558 pends particulate matter, emerges as the agent that most likely controls the Chla vari-

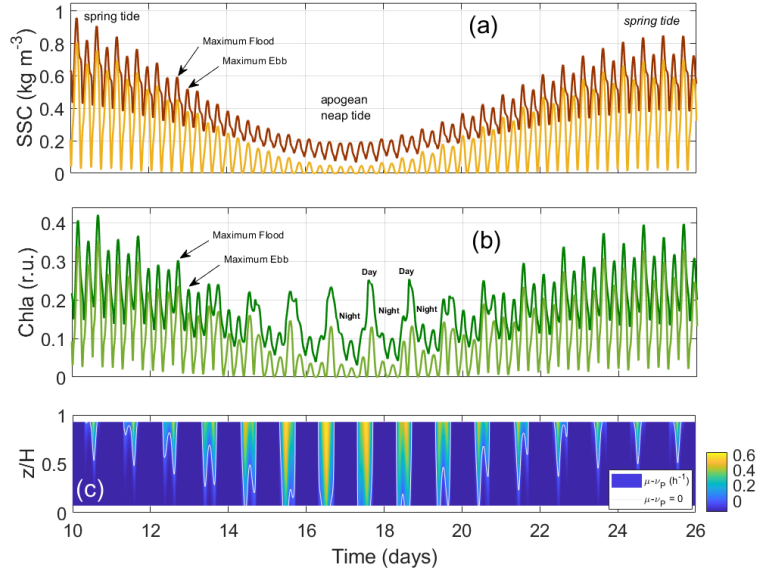


Figure 8. Model output at the spring-neap and tidal scale. Time series of SSC (panel a) and Chla concentration (panel b) near the bed at $z/H = 0.93$ (dark-colored curves) and near the surface at $z/H = 0.07$ (light-colored curves). Panel c shows a $z-t$ color plot of the net specific growth rate. The light grey curve in panel c is the contour line of zero net specific growth rate. Time is presented in days from 10/10/09.

559 ability (panel b). This phenomenon occurs in the GRE during most of the analysis pe-
 560 riod (Section 3.1). Lags between relative Chla maxima near the surface (panel b, light
 561 green curve) and near the bottom (panel b, dark green curve) are similar to those for
 562 SSC (panel a). Modeled Chla concentrations are higher for larger depths, which is con-
 563 sistent with observations. For this experiment, the sinking velocity of P that best mim-
 564 ics observations is $w_{s,P} = 3.5 \cdot 10^{-4} \text{ m s}^{-1}$. This value is at least one order of magni-
 565 tude larger than that for pelagic algal cells (e.g., Sarthou et al. (2005); Liu et al. (2018)).
 566 This finding strongly suggests that the in-phase oscillations of Chla and SSC observed
 567 during low flows are caused by the attachment of a significant fraction of the phytoplankton
 568 biomass to sediment particles, thereby increasing the effective sinking velocity of P .

569 During the apogean neap tide that occurs at approximately day 18 in Fig. 8, the
 570 tidal current decreases and light availability increases because of the overall settling of
 571 particulate matter (including the Chla-containing biomass attached to sediment parti-
 572 cles). As a result, the net specific growth rate increases and even becomes positive through-
 573 out the water column during day times around slack tides (panel c). In such cases, the
 574 Chla-concentration time series are temporally uncorrelated with the SSC and the radiation-
 575 Chla relationship becomes evident (panel b). During those periods, light-mediated growth
 576 of phytoplankton increases and the remaining Chla-containing biomass in the water col-
 577 umn varies more significantly according to the daily radiative forcing.

578 4 Discussion

579 4.1 Seasonal Variability

580 Results of model experiments show that overall, for the range of maximum specific
 581 growth rates explored, the net specific growth rate of phytoplankton contributes nega-
 582 tively to the local storage of P in the water column at the seasonal scale, even during
 583 summers when the incoming radiation is larger than average and light-mediated growth

584 increases (Fig. 7). The negative local net specific growth rate, in addition to the neg-
 585 ative contribution by sinking, must be compensated by the vertical diffusive fluxes of Chla
 586 from the bottom. This situation mimics observations of Chla in the lower part of the es-
 587 tuary. Observations of the seasonal variations of Chla concentration in the lower part
 588 of the estuary are better described by maximum specific growth rates of $\mu_{\max} = 0.10 \text{ h}^{-1}$.
 589 Only when simulations were performed without considering the shading effects by sed-
 590 iments, i.e., light was allowed to penetrate deeper in the water column, a positive con-
 591 tribution of the net specific growth rate to the local storage of phytoplankton was found.
 592 In a nutrient-rich estuary, these findings demonstrate the important role of the inhibi-
 593 tion of growth due to the attenuation of light by high SSC levels and agree with the di-
 594 agnosis of the GRE by Ruiz et al. (2017). These authors pointed to an estuary domi-
 595 nated by high decay or grazing rates of organic matter not compensated by primary pro-
 596 duction, which is limited by high turbidity. In fact, the model considers Chla growth as
 597 only restricted by light availability, not by nutrients or temperature, although the tempera-
 598 ture-dependence of μ_{\max} is important at the seasonal time scale. This restriction is based on
 599 the actual conditions within the Guadalquivir estuary, in which the attenuation of light
 600 by turbidity is the dominant limiting factor for growth (Ruiz et al., 2013, 2017). The growth-
 601 limiting term was modeled following Arndt et al. (2007), but other available formula-
 602 tions for this term are also suitable. The expression $\mu = \mu_{\max} I / (I + I_L)$ used by a num-
 603 ber of authors (e.g., Huisman et al. (2006)), with the half-saturation constant I_L , was
 604 tested and was also capable of capturing the Chla behavior in the GRE. Processes such
 605 as grazing and natural decay are lumped in the specific loss rate parameter ν_P , which
 606 is assumed to be constant, although its dependence on temperature is also relevant at
 607 seasonal scale. Nevertheless, the value considered (Table 1) is within the typical range
 608 of values used in the literature (e.g., Sarthou et al. (2005)).

609 Additionally, observations suggested that, in addition to the inhibition of light pen-
 610 etration by high SSC, the inner shelf conditions and loads from the catchment may af-
 611 fect the along-channel distribution of SSC and Chla concentrations at the seasonal scale.
 612 During the dry season (summer), the highest Chla values were observed near the mouth
 613 (Fig. 3, panel e). This situation was due to winds that favor upwelling, lower fresh wa-
 614 ter discharges and improved light conditions due to lower turbidity and higher radiation
 615 values (Prieto et al., 2009; Caballero & Navarro, 2018). Mean concentrations of Chla de-
 616 creased upstream, while turbidity increased. This finding was consistent with the limi-
 617 tation of primary production by turbidity. In contrast, during the wet season, both SSC
 618 and Chla concentration showed larger values upstream than those at the mouth, espe-
 619 cially after specific high discharge events. Seasonal Chla concentrations near the mouth
 620 thus had a six-month lag compared with those in the upper parts of the estuary. The
 621 approximate threshold location at 20 km roughly coincided with the maximum salinity
 622 gradient during low flows and a region of tight channel curvature (Fig. 1). Similar sea-
 623 sonal variations in the along-channel distribution of Chla were observed in other estu-
 624 aries (e.g., Roegner et al. (2011)).

625 4.2 Spring-Neap and Tidal Variability

626 At spring-neap and tidal scales, analysis of the observations reveals strong posi-
 627 tive correlations between SSC and Chla during most of the tidal cycles under normal con-
 628 ditions (Figs. 5 and 6). The M2 and M4 tidal phases of the SSC and Chla had almost
 629 exactly the same values in the estuary, except at the station near the mouth, which was
 630 most likely controlled by the climate conditions at the inner shelf (Caballero & Navarro,
 631 2018). The idealized model helps to explain the observed positive correlation between
 632 SSC and Chla (Fig. 8). The model points to a local generation within the estuary of both
 633 SSC and Chla, in which their simultaneous increases were related to resuspension induced
 634 by tidal shear stress. Satisfactory results were obtained when assuming that the tides
 635 comprised only the main semidiurnal tidal constituents (M2, S2, and N2) and their most
 636 energetic overtides (M4, MS4, and MN4) and that the effective settling velocity of Chla

637 was 10% to 50% lower than that of SSC ($w_{s,P} = 3.5 \cdot 10^{-4} \text{ m s}^{-1}$). This relatively large
 638 value of the effective settling velocity $w_{s,P}$, as compared to other values for algal cells
 639 (e.g., Sarthou et al. (2005); Liu et al. (2018)), supports the hypothesis that a significant
 640 portion of the Chla-containing biomass was aggregated with the suspended sediments.
 641 The settling velocity of Chla is an effective parameter in the model that lumps differ-
 642 ent species, both free or attached to sediments. The fraction of attached Chla-containing
 643 biomass was controlled in the model through the effective settling velocity of Chla. Larger
 644 values of $w_{s,P}$ suggest that a larger amount of Chla is aggregated with the suspended
 645 sediments, which typically have larger settling velocities than algae. Therefore, the in-
 646 phase oscillations at the spring-neap and tidal scales of Chla and SSC were likely due
 647 to the attachment of algal species, such as microphytobenthos, to sediment particles. A
 648 substantial part of the observed Chla-containing biomass could thus be resuspended by
 649 tides in the shoals where they grew. Once resuspended, lateral mixing processes may have
 650 caused them to be transported into the channel, where measurements were made. As the
 651 GRE is a narrow and highly-energetic estuary, this process could favor the existence of
 652 a resident shoal-derived benthic microalgae population in the channel that is subject to
 653 sinking and resuspension mechanisms.

654 There is evidence in other estuaries and coastal areas that tidally-induced suspended
 655 sediments convey Chla-containing biomass. Colijn and de Jonge (1984) estimated the
 656 annual primary production from Chla content in sediments in the Ems-Dollard estuary.
 657 de Jonge and van Beusekom (1995) found that mud and microphytobenthos were resus-
 658 pended simultaneously from shoals in the Scheldt estuary by erosion due to wind waves.
 659 Irigoien and Castel (1997) suggested that a significant percentage of the measured chloro-
 660 phyll at the ETM in the Gironde estuary was originated from resuspended microphy-
 661 tobenthos, whose concentration exhibited a remarkable correlation with the SSC. de Lo-
 662 mas et al. (2005) detected tidal variations of microphytobenthos in sediments in the wa-
 663 ter column in the estuarine environment of the Bay of Cádiz. In the North Sea, Blauw
 664 et al. (2012) observed in-phase oscillations of Chla and SSC on a fortnightly time-scale
 665 that were driven by tide-induced turbulent mixing. These authors attributed this be-
 666 havior to alternating periods of sinking and resuspension of algal cells and SSC. Further-
 667 more, de Jong and de Jonge (1995) and C. H. Lucas et al. (2000) recognized that, over
 668 short time scales, water column productivity in reduced-productivity turbid estuaries
 669 may be dominated by resuspended microphytobenthos in response to increases in cur-
 670 rents, as the free phytoplankton growth is light-limited.

671 Based on the observations, there was a significant correlation between the day-night
 672 solar radiation cycle and the Chla concentration signal that emerged at some weak (apogean)
 673 neap tides. Similar observations were also reported by Blauw et al. (2012) in the North
 674 Sea shelf. This predominant diurnal oscillation coincided with a strong decline in tidal
 675 currents and thus in suspended particulate matter. This variability may be indicative
 676 of two processes that are not mutually exclusive. First, the temporal decoupling between
 677 Chla and SSC might suggest that the growth of part of the Chla-containing biomass still
 678 remaining in the water column was driven by the day-night radiative cycle. According
 679 to the model results, during those periods, tidal shear stress decreased, causing a strong
 680 decline in SSC (and phytoplankton biomass attached to sediments) and an increase in
 681 specific growth rates, especially near the surface where light availability was highest (Fig. 8).
 682 The moment at which the peaks of Chla values were observed (i.e., the occurrence of great-
 683 est growth) depended on the relative phase between the 24 h solar radiation forcing and
 684 the oscillation in SSC associated with changes in the mixing and distribution of suspended
 685 matter. Another plausible hypothesis that may explain this behavior is that cells in the
 686 water column adapt to the increase in light. Changes in cell physiology and metabolism
 687 (e.g., changes in their Chla pigment content) may partially compensate for changes in
 688 light intensity by optimizing their ability to harvest light when it is available (Falkowski,
 689 1980). In addition, day-night changes in the vertical thermal structure could also induce
 690 a diurnal periodicity in growth. However, this did not seem to be the case in the GRE,

691 given that the temperature stratification in the GRE during normal conditions was very
692 weak.

693 4.3 Variability prior and after High-discharge Events

694 Field data show that the response of SSC and Chla concentration to high fresh-
695 water discharge depends on the magnitude of the river flow (Fig. 3). After a high-discharge
696 event of $531 \text{ m}^3\text{s}^{-1}$ (event 1), extremely high values of Chla-containing matter and SSC
697 occurred, which were subsequently modulated by the spring-neap cycle. The location of
698 the relative along-channel maximum of Chla ($x \approx 35 \text{ km}$) may be dependent on the mag-
699 nitude of the discharge, i.e., higher river flows advect the Chla maximum further down-
700 stream, and possibly depended on the consumption rates of organic material (Liu & de
701 Swart, 2015). As pointed out by Ruiz et al. (2015), the consumption of the organic mat-
702 ter by heterotrophic processes produced the oxygen depletion. This consumption rate
703 was not compensated by primary production, which was prevented by the high SSC in
704 the estuary. The high-discharge event also led to the amplification of tidal currents, prob-
705 ably due to the suppression of turbulence by the suspended sediment stratification (Wang
706 et al., 2014; Losada et al., 2017), which in turn helped to keep the suspended matter longer
707 in the water column.

708 High-discharge events of lower order of magnitude (e.g., event 2 with peak of $91 \text{ m}^3\text{s}^{-1}$)
709 did not have a remarkable impact on tidal currents and SSC, including the location and
710 intensity of the ETM. The sediment delivered or eroded from the estuary bed by these
711 discharges was apparently small. However, a few days prior to high-discharge event 2,
712 high Chla concentrations were observed in the upper part of the estuary ($x \approx 60 \text{ km}$).
713 At present, and with the available data, there is no satisfactory explanation of this phe-
714 nomenon. The freshwater release from the Alcalá del Río dam did not seem to be the
715 triggering factor. Other secondary tributaries might have contributed to the overall dis-
716 charge and the triggering of the enhanced Chla-containing biomass concentrations prior
717 and after event 2. The high Chla concentrations were not a manifestation of a phyto-
718 plankton bloom induced by an extra input of nutrients, which were already high in the
719 estuary. The role of stratification should be also discarded as a possible mechanism, given
720 that the water column where the high Chla concentration values were observed was well-
721 mixed. To identify the triggering mechanism(s) of the bloom prior and after event 2 re-
722 quires further study.

723 4.4 Model Performance

724 Although the model captures key aspects of the SSC-Chla variability, important
725 simplifications are considered and should be mentioned. Regarding abiotic conditions,
726 this is a one-dimensional water column model. Thus, longitudinal processes are not ex-
727 plicitly considered. Tides are only included as a source of vertical mixing and shear stress
728 at the bottom. The turbulent mixing, parametrized in the model by means of an eddy
729 diffusivity coefficient, is assumed to be uniform in the vertical direction, although it evolves
730 over time. The time-dependence due to tidal action and SSC is included in the coeffi-
731 cient by means of a bulk-type Richardson number. Salinity stratification, which is nor-
732 mally weak in the GRE, was kept constant in all the experiments. Nevertheless, changes
733 in salinity stratification are known to affect turbulence, the vertical structure of which
734 may influence phytoplankton density patterns in estuaries (Liu & de Swart, 2018). More-
735 over, lateral processes that transport biomass from the tidal flats, where it grows, into
736 the main channel are neglected, although they are recognized as crucial for reproduc-
737 ing the details of the phytoplankton dynamics in many estuaries (May et al., 2003). The
738 study of the role of shoals in SSC-Chla relationships and the extension of the model to
739 include lateral processes will be addressed in future investigations.

740 Finally, although many biotic and physical processes are not accounted for in the
 741 model, it was able to reproduce and explain close connections observed between Chla
 742 and SSC. The model successfully identified basic mechanisms that may control the be-
 743 havior of Chla-containing biomass and SSC in the GRE. Like many other idealized mod-
 744 els, the model used here is flexible, has a low computational cost and helps to gain in-
 745 sight in the dynamics of turbid estuaries. Even though the modeling study focused on
 746 Guadalquivir estuary observations, the model could also help to explain phenomena in
 747 other highly turbid and high-nutrient estuaries.

748 5 Conclusions

749 This study contributes to further understanding of the relationships between SSC
 750 and Chla, which are well-known indicators of the health of estuarine environments, in
 751 nutrient-rich but reduced-productivity environments such as the Guadalquivir estuary.
 752 Answers to the three research questions of this study have been provided, which trans-
 753 late into the following conclusions.

754 The net specific growth rate of Chla-containing biomass is inhibited by turbidity
 755 throughout the year. Results of model results indicate that overall, even during summer-
 756 time, the net specific growth rate contributes negatively to its local storage due to the
 757 high SSC levels. The negative local net specific growth rate, in addition to the negative
 758 contribution by settling, is only compensated by the vertical diffusive fluxes of Chla. The
 759 stretches closest to the mouth exhibited larger Chla concentration during the summer
 760 period characterized by winds favorable to upwelling and improved light conditions. Up-
 761 stream stretches show the opposite behavior: larger Chla concentration during the wet
 762 season. Local maxima of averaged Chla levels were observed between the two ETMs, namely,
 763 at locations with relatively low SSC values.

764 The model identified possible mechanisms that might explain the observed in-phase
 765 fluctuations of SSC and Chla at spring-neap and tidal scales (M2 and M4 tidal phases
 766 of SSC and Chla were similar). These fluctuations occur throughout most of the obser-
 767 vation period during low river flows and their decoupling at some apogean neap tides.
 768 The simultaneous resuspension of sediments and Chla-containing biomass induced by
 769 tidal shear stress seems to be the major process that causes the SSC and Chla concen-
 770 trations to exhibit a strong positive correlation that persists most of the year during low
 771 river flows. The relatively large values of settling velocities of Chla that ensue from the
 772 model results indicate that a substantial amount of Chla-containing biomass in the wa-
 773 ter column is likely composed of algal species of phytoplankton that are attached to sed-
 774 iments. Therefore, although net photosynthetic production is relatively low due to the
 775 light attenuation by turbidity, over spring-neap and tidal scales, resuspended microal-
 776 gae may make a notable contribution to water column productivity. At certain apogean
 777 neap tides, when bed shear stress weakens, particulate matter tends to sink. In such cases,
 778 light availability notably improves in the upper layers of the water column, light-mediated
 779 growth of phytoplankton increases and the Chla concentration instead varies according
 780 to the day-night radiation cycle.

781 Appendix A Numerical Scheme

782 The Chla concentration and SSC fields, P and c , respectively, are obtained by in-
 783 tegrating numerically Eqs. 1a and 1b. The vertical coordinate and time are partitioned
 784 defining a spacing Δz and a time step Δt , respectively. This results in $z_j = j\Delta z$, with
 785 $j = 0, 1, 2, \dots, N_z - 1$, with $H = (N_z - 1)\Delta z$, and $t^n = n\Delta t$, with $n = 0, 1, 2, \dots, N_t -$
 786 1 , where $(N_t - 1)\Delta t$ is a given final time. Accordingly, $\xi_j^n \equiv \xi(z_j, t^n)$ for any variable
 787 $\xi(x, t)$. In particular, $P_j^n \equiv P(z_j, t^n)$ and $c_j^n \equiv c(z_j, t^n)$. Equations 1a and 1b are then
 788 discretized by means of finite differences and numerically resolved. An explicit forward
 789 in time scheme, combined with a centered finite difference scheme in the vertical coor-

790 dinate, is used here for Eqs. 1a and 1b. Backward and forward finite differences are used
 791 to approximate the surface and bottom boundary conditions Eqs. 6a-6d, respectively.
 792 The iterative expressions for the governing equations of P and c read, respectively,

$$P_j^{n+1} = P_j^n + \Delta t \left[(\mu_j^n - \nu_P) P_j^n - \frac{w_{s,P}}{2\Delta z} (P_{j+1}^n - P_{j-1}^n) + \left(\frac{K_v^n}{\Delta z^2} \right) (P_{j+1}^n - 2P_j^n + P_{j-1}^n) \right] \quad (\text{A1a})$$

$$c_j^{n+1} = c_j^n + \Delta t \left[-\frac{w_{s,c}}{2\Delta z} (c_{j+1}^n - c_{j-1}^n) + \left(\frac{K_v^n}{\Delta z^2} \right) (c_{j+1}^n - 2c_j^n + c_{j-1}^n) \right], \quad (\text{A1b})$$

796 with $K_v^n \equiv K_v(t^n)$ (from Eqs. 8 and 9). The specific growth rate is obtained from Eq. 2
 797 as $\mu_j^n = \mu_{\max} [1 - \exp(-e_P I_j^n)]$ where

$$I_j^n = \Omega^n \exp \left(-\kappa_w z_j - \kappa_P \Delta z \sum_{q=0}^j P_q^n - \kappa_{\text{SSC}} \Delta z \sum_{q=0}^j c_q^n \right), \quad (\text{A2})$$

798 where Ω^n are determined from Eq. 4, evaluated at times t^n .

799 The discretized versions of the boundary conditions at the surface, i.e., Eqs. 6a and
 800 6b, are

$$P_0^n = P_1^n \left(1 - \frac{w_{s,P} \Delta z}{K_v^n} \right), \quad (\text{A3a})$$

$$c_0^n = c_1^n \left(1 - \frac{w_{s,c} \Delta z}{K_v^n} \right). \quad (\text{A3b})$$

804 Those for the boundary conditions at the bottom, Eqs. 6c and 6d, read

$$P_{N_z-1}^n = P_{N_z-2}^n + \frac{\Delta z}{K_v^n} b_P \max\{\tau_{b,N_z-2}^n - \tau_{c,N_z-2}^n, 0\}, \quad (\text{A4a})$$

$$c_{N_z-1}^n = c_{N_z-2}^n + \frac{\Delta z}{K_v^n} b_c \max\{\tau_{b,N_z-2}^n - \tau_{c,N_z-2}^n, 0\}. \quad (\text{A4b})$$

808 In these expressions, the shear stresses are determined from Eqs. 7a and 7b as $\tau_{b,N_z-2}^n =$
 809 $C_D \rho_{N_z-2}^n (u^n)^2$ and $\tau_{c,N_z-2}^n = \alpha_1 (m^n - \alpha_2)$, with $m^n = \Delta z \sum_{q=1, N_z-2} c_q^n$.

810 Finally, the numerical scheme is stable if the time step size obeys

$$\Delta t < \min \left(\frac{\Delta z^2}{2 \max_n \{K_v^n\}}, 2 \max_n \{K_v^n\} / \max(w_{s,P}, w_{s,c})^2 \right). \quad (\text{A5})$$

811 During the iteration procedure, the SSC equation A1b is solved first, and its result is used
 812 to solve Eq. A1a.

813 Acknowledgments

814 Part of this research was conducted by MDM during a three-month visit in 2017 to Utrecht
 815 University (UU). MDM was supported by the Program *José Castillejo* of the Plan Es-
 816 tatal de Investigación Científica y de Innovación 2013-2016 en I+D+i, Spanish Ministry
 817 of Education, Culture, and Sports (Ref. CAS17-00247). MDM would also like to acknowl-
 818 edge support for this work from other research funding programs: Programa Estatal de
 819 Investigación, Desarrollo e Innovación orientada a los RETOS de la sociedad (Ref. CTM2017-
 820 89531-R); and Ayudas de la Fundación Biodiversidad, del Ministerio de Agricultura y
 821 Pesca, Alimentación y Medio Ambiente, para la realización de proyectos en materia de
 822 adaptación al cambio climático (Ref. PRCV00487). Data described in this work are avail-
 823 able from <https://doi.org/10.5281/zenodo.3459610> (CC BY 4.0 license). MDM would
 824 like to thank all GDFA members for their back-up at Granada during the time of his visit
 825 to UU. The authors would also like to thank Bo Liu, Victor N. de Jonge, and Javier Ruiz
 826 for fruitful discussions, and to Ángel Rodríguez Lozano, scientific director of the web por-
 827 tal <http://cienciaes.com/>, for the public outreach of this work. Finally, the authors
 828 are indebted to the Editors and two anonymous reviewers for their comments, which helped
 829 to greatly improve this paper.

References

- Arndt, S., Vanderborght, J.-P., & Regnier, P. (2007). Diatom growth response to physical forcing in a macrotidal estuary: Coupling hydrodynamics, sediment transport, and biogeochemistry. *Journal of Geophysical Research: Oceans*, *112*(C5).
- Azevedo, I. C., Bordalo, A. A., & Duarte, P. (2014). Influence of freshwater inflow variability on the Douro estuary primary productivity: A modelling study. *Ecological Modelling*, *272*, 1–15.
- Blauw, A. N., Beninca, E., Laane, R. W. P. M., Greenwood, N., & Huisman, J. (2012). Dancing with the tides: Fluctuations of coastal phytoplankton orchestrated by different oscillatory modes of the tidal cycle. *PLoS ONE*, *7*(11), e49319.
- Bowden, K., Fairbairn, L., & Hughes, P. (1959). The distribution of shearing stresses in a tidal current. *Geophysical Journal International*, *2*(4), 288–305.
- Boyer, J. N., Kelble, C. R., Ortner, P. B., & Rudnick, D. T. (2009). Phytoplankton bloom status: Chlorophyll a biomass as an indicator of water quality condition in the southern estuaries of Florida, USA. *Ecological Indicators*, *9*(6), S56–S67.
- Branco, A. B., & Kremer, J. N. (2005). The relative importance of chlorophyll and colored dissolved organic matter (CDOM) to the prediction of the diffuse attenuation coefficient in shallow estuaries. *Estuaries and Coasts*, *28*(5), 643–652.
- Caballero, I., & Navarro, G. (2018). Application of extended full resolution MERIS imagery to assist coastal management of the area adjacent to the Guadalquivir estuary. *Progress in Oceanography*, *165*, 215–232.
- Cloern, J. E. (1996). Phytoplankton bloom dynamics in coastal ecosystems: A review with some general lessons from sustained investigation of San Francisco Bay, California. *Reviews of Geophysics*, *34*(2), 127–168.
- Cloern, J. E., Foster, S. Q., & Kleckner, A. E. (2014). Phytoplankton primary production in the world’s estuarine-coastal ecosystems. *Biogeosciences*, *11*(9), 2477–2501.
- Colijn, F., & de Jonge, V. N. (1984). Primary production of microphytobenthos in the Ems-Dollard Estuary. *Marine Ecology Progress Series*, *14*(2), 185–196.
- de Jong, D. J., & de Jonge, V. N. (1995). Dynamics and distribution of microphytobenthic chlorophyll-a in the Western Scheldt estuary (SW Netherlands). *Hydrobiologia*, *311*(1), 21–30.
- de Jonge, V. N., Schuttelaars, H. M., van Beusekom, J. E., Talke, S. A., & de Swart, H. E. (2014). The influence of channel deepening on estuarine turbidity levels and dynamics, as exemplified by the ems estuary. *Estuarine, Coastal and Shelf Science*, *139*, 46–59.
- de Jonge, V. N., & van Beusekom, J. E. E. (1995). Wind-and tide-induced resuspension of sediment and microphytobenthos from tidal flats in the Ems estuary. *Limnology and Oceanography*, *40*(4), 776–778.
- de Lomas, J. G., Corzo, A., Garcia, C. M., & van Bergeijk, S. A. (2005). Microbenthos in a hypersaline tidal lagoon: factors affecting microhabitat, community structure and mass exchange at the sediment-water interface. *Aquatic Microbial Ecology*, *38*(1), 53–69.
- de Swart, H. E., Schuttelaars, H. M., & Talke, S. A. (2009). Initial growth of phytoplankton in turbid estuaries: A simple model. *Continental Shelf Research*, *29*(1), 136–147.
- Díez-Minguito, M., Baquerizo, A., de Swart, H. E., & Losada, M. A. (2014). Structure of the turbidity field in the Guadalquivir estuary: Analysis of observations and a box model approach. *Journal of Geophysical Research: Oceans*, *119*(10), 7190–7204.

- 884 Díez-Minguito, M., Baquerizo, A., Ortega-Sánchez, M., Navarro, G., & Losada,
885 M. A. (2012). Tide transformation in the Guadalquivir estuary (SW Spain)
886 and process-based zonation. *Journal of Geophysical Research: Oceans (1978–*
887 *2012)*, *117*(C3).
- 888 Díez-Minguito, M., Contreras, E., Polo, M. J., & Losada, M. A. (2013). Spatio-
889 temporal distribution, along-channel transport, and post-riverflood recovery
890 of salinity in the Guadalquivir estuary (SW Spain). *Journal of Geophysical*
891 *Research: Oceans*, *118*(5), 2267–2278.
- 892 Dronkers, J. J. (1964). *Tidal computations in rivers and coastal waters*. North-
893 Holland, Amsterdam.
- 894 Falkowski, P. G. (1980). Light-shade adaptation in marine phytoplankton. In *Pri-*
895 *mary productivity in the sea* (pp. 99–119). Springer.
- 896 Fisher, T. R., Harding, L. W., Stanley, D. W., & Ward, L. G. (1988). Phyto-
897 plankton, nutrients, and turbidity in the Chesapeake, Delaware, and Hudson
898 estuaries. *Estuarine, Coastal and Shelf Science*, *27*(1), 61–93.
- 899 García-Lafuente, J., Delgado, J., Navarro, G., Calero, C., Díez-Minguito, M., Ruiz,
900 J., & Sánchez-Garrido, J. C. (2012). About the tidal oscillations of temper-
901 ature in a tidally driven estuary: The case of Guadalquivir estuary, southwest
902 Spain. *Estuarine, Coastal and Shelf Science*, *111*, 60–66.
- 903 Geyer, W. R., Trowbridge, J. H., & Bowen, M. M. (2000). The dynamics of a par-
904 tially mixed estuary. *Journal of Physical Oceanography*, *30*(8), 2035–2048.
- 905 González-Ortegón, E., & Drake, P. (2012). Effects of freshwater inputs on the
906 lower trophic levels of a temperate estuary: physical, physiological or trophic
907 forcing? *Aquatic Sciences*, *74*(3), 455–469.
- 908 Grinsted, A., Moore, J. C., & Jevrejeva, S. (2004). Application of the cross wavelet
909 transform and wavelet coherence to geophysical time series. *Nonlinear Pro-*
910 *cesses in Geophysics*, *11*(5/6), 561–566.
- 911 Huijts, K. M. H., Schuttelaars, H. M., de Swart, H. E., & Valle-Levinson, A. (2006).
912 Lateral entrapment of sediment in tidal estuaries: An idealized model study.
913 *Journal of Geophysical Research: Oceans*, *111*(C12).
- 914 Huisman, J., Thi, N. N. P., Karl, D. M., & Sommeijer, B. (2006). Reduced mixing
915 generates oscillations and chaos in the oceanic deep chlorophyll maximum. *Nat-*
916 *ure*, *439*(7074), 322.
- 917 Irigoien, X., & Castel, J. (1997). Light limitation and distribution of chlorophyll
918 pigments in a highly turbid estuary: the Gironde (SW France). *Estuarine,*
919 *Coastal and Shelf Science*, *44*(4), 507–517.
- 920 Lajaunie-Salla, K., Wild-Allen, K., Sottolichio, A., Thouvenin, B., Litrico, X., &
921 Abril, G. (2017). Impact of urban effluents on summer hypoxia in the highly
922 turbid Gironde estuary, applying a 3D model coupling hydrodynamics, sed-
923 iment transport and biogeochemical processes. *Journal of Marine Systems*,
924 *174*, 89–105.
- 925 Liu, B., & de Swart, H. E. (2015). Impact of river discharge on phytoplankton
926 bloom dynamics in eutrophic estuaries: A model study. *Journal of Marine Sys-*
927 *tems*, *152*, 64–74.
- 928 Liu, B., & de Swart, H. E. (2018). Quantifying the effect of salinity stratification on
929 phytoplankton density patterns in estuaries. *Estuaries and Coasts*, *41*(2), 453–
930 470.
- 931 Liu, B., de Swart, H. E., & de Jonge, V. N. (2018). Phytoplankton bloom dynamics
932 in turbid, well-mixed estuaries: A model study. *Estuarine, Coastal and Shelf*
933 *Science*, *211*, 137–151.
- 934 Losada, M. A., Díez-Minguito, M., & Reyes-Merlo, M. Á. (2017). Tidal-fluvial inter-
935 action in the Guadalquivir River Estuary: Spatial and frequency-dependent re-
936 sponse of currents and water levels. *Journal of Geophysical Research: Oceans*,
937 *122*(2), 847–865.
- 938 Lucas, C. H., Widdows, J., Brinsley, M. D., Salkeld, P. N., & Herman, P. M. (2000).

- 939 Benthic-pelagic exchange of microalgae at a tidal flat. 1. pigment analysis. *Ma-*
 940 *rine Ecology Progress Series*, 59–73.
- 941 Lucas, L. V., & Cloern, J. E. (2002). Effects of tidal shallowing and deepening on
 942 phytoplankton production dynamics: A modeling study. *Estuaries*, 25(4), 497–
 943 507.
- 944 Lucas, L. V., Thompson, J. K., & Brown, L. R. (2009). Why are diverse relation-
 945 ships observed between phytoplankton biomass and transport time? *Limnology*
 946 *and Oceanography*, 54(1), 381–390.
- 947 May, C. L., Koseff, J. R., Lucas, L. V., Cloern, J. E., & Schoellhamer, D. H. (2003).
 948 Effects of spatial and temporal variability of turbidity on phytoplankton
 949 blooms. *Marine Ecology Progress Series*, 254, 111–128.
- 950 McSweeney, J. M., Chant, R. J., Wilkin, J. L., & Sommerfield, C. K. (2017).
 951 Suspended-sediment impacts on light-limited productivity in the Delaware
 952 estuary. *Estuaries and Coasts*, 40(4), 977–993.
- 953 Monismith, S. G., Burau, J. R., & Stacey, M. (1996). Stratification dynamics and
 954 gravitational circulation in northern San Francisco Bay. In J. T. Hollibaugh
 955 (Ed.), *San Francisco Bay: The Ecosystem* (pp. 123–153). American Associa-
 956 tion for the Advancement of Science.
- 957 Munk, W., & Anderson, E. (1948). Notes on a theory of the thermocline. *Journal of*
 958 *Marine Research*, 7, 276–295.
- 959 Muylaert, K., & Sabbe, K. (1999). Spring phytoplankton assemblages in and
 960 around the maximum turbidity zone of the estuaries of the Elbe (Germany),
 961 the Schelde (Belgium/The Netherlands) and the Gironde (France). *Journal of*
 962 *Marine Systems*, 22(2-3), 133–149.
- 963 Muylaert, K., Van Wichelen, J., Sabbe, K., & Vyverman, W. (2001). Effects of
 964 freshets on phyto-plankton dynamics in a freshwater tidal estuary (Schelde,
 965 Belgium). *Archiv fur Hydrobiologie*, 150(2), 269–288.
- 966 Navarro, G., Gutierrez, F. J., Díez-Minguito, M., Losada, M. A., & Ruiz, J. (2011).
 967 Temporal and spatial variability in the Guadalquivir Estuary: A challenge for
 968 real-time telemetry. *Ocean Dynamics*, 61(6), 753–765.
- 969 Pawlowicz, R., Beardsley, B., & Lentz, S. (2002). Classical tidal harmonic anal-
 970 ysis including error estimates in MATLAB using T_TIDE. *Computers & Geo-*
 971 *sciences*, 28, 929–937.
- 972 Prieto, L., Navarro, G., Rodríguez-Gálvez, S., Huertas, I. E., Naranjo, J. M., &
 973 Ruiz, J. (2009). Oceanographic and meteorological forcing of the pelagic
 974 ecosystem on the Gulf of Cádiz shelf (SW Iberian Peninsula). *Continental*
 975 *Shelf Research*, 29(17), 2122–2137.
- 976 Roegner, G. C., Seaton, C., & Baptista, A. M. (2011). Climatic and tidal forcing
 977 of hydrography and chlorophyll concentrations in the Columbia River estuary.
 978 *Estuaries and Coasts*, 34(2), 281–296.
- 979 Ruiz, J., Macías, D., Losada, M. A., Díez-Minguito, M., & Prieto, L. (2013). A sim-
 980 ple biogeochemical model for estuaries with high sediment loads: Application
 981 to the Guadalquivir River (SW Iberia). *Ecological Modelling*, 265, 194–206.
- 982 Ruiz, J., Macías, D., & Navarro, G. (2017). Natural forcings on a transformed terri-
 983 tory overshoot thresholds of primary productivity in the Guadalquivir estuary.
 984 *Continental Shelf Research*, 148, 199–207.
- 985 Ruiz, J., Polo, M. J., Díez-Minguito, M., Navarro, G., Morris, E. P., Huertas, E., . . .
 986 Losada, M. A. (2015). The Guadalquivir estuary: A hot spot for environmen-
 987 tal and human conflicts. In C. W. Finkl & C. Makowski (Eds.), *Environmental*
 988 *management and governance* (Vol. 8, p. 199–232). Springer.
- 989 Sanford, L. P., & Halka, J. P. (1993). Assessing the paradigm of mutually exclusive
 990 erosion and deposition of mud, with examples from upper Chesapeake Bay.
 991 *Marine Geology*, 114(1-2), 37–57.
- 992 Sarthou, G., Timmermans, K. R., Blain, S., & Tréguer, P. (2005). Growth physiol-
 993 ogy and fate of diatoms in the ocean: a review. *Journal of Sea Research*, 53(1–

- 994 2), 25–42.
- 995 Son, M., & Hsu, T.-J. (2011). The effects of flocculation and bed erodibility on
996 modeling cohesive sediment resuspension. *Journal of Geophysical Research:*
997 *Oceans*, *116*(C3).
- 998 Stacey, M. T., & Ralston, D. K. (2005). The scaling and structure of the estuarine
999 bottom boundary layer. *Journal of Physical Oceanography*, *35*(1), 55–71.
- 1000 Uncles, R. J., Hooper, T., Stephens, J., & Harris, C. (2018). Seasonal variability of
1001 turbidity, salinity, temperature and suspended chlorophyll in a strongly tidal
1002 sub-estuary: The Lynher Marine Conservation Zone. *Estuarine, Coastal and*
1003 *Shelf Science*, *212*, 253–264.
- 1004 Wang, Z. B., Winterwerp, J. C., & He, Q. (2014). Interaction between suspended
1005 sediment and tidal amplification in the Guadalquivir Estuary. *Ocean Dynam-*
1006 *ics*, *64*(10), 1487–1498.
- 1007 Winterwerp, J. C., & van Kesteren, W. G. M. (2004). *Introduction to the physics of*
1008 *cohesive sediment dynamics in the marine environment* (Vol. 56). Elsevier.